JBO Journal of Biomedical Optics

RESEARCH PAPER

In situ pulmonary mucus hydration assay using rotational and translational diffusion of gold nanorods with polarization-sensitive optical coherence tomography

Kelsey J. Oeler,[a] Richard L. Blackmon,[b] Silvia M. Kreda,[c] Taylor Robinson,[d] Melanie Ghelardini,[e] Brian S. Chapman,[e] Joseph Tracy,[e] David B. Hill,[a,c] and Amy L. Oldenburg[a,d,*]

[a]University of North Carolina at Chapel Hill, Department of Biomedical Engineering, Chapel Hill, North Carolina, United States
[b]Elon University, Department of Engineering, Elon, North Carolina, United States
[c]University of North Carolina at Chapel Hill, Marsico Lung Institute/Cystic Fibrosis/Pulmonary Research and Treatment Center, Chapel Hill, North Carolina, United States
[d]University of North Carolina at Chapel Hill, Department of Physics and Astronomy, Chapel Hill, North Carolina, United States
[e]North Carolina State University, Department of Materials Science and Engineering, Raleigh, North Carolina, United States

ABSTRACT. **Significance:** Assessing the nanostructure of polymer solutions and biofluids is broadly useful for understanding drug delivery and disease progression and for monitoring therapy.

Aim: Our objective is to quantify bronchial mucus solids concentration (wt. %) during hypertonic saline (HTS) treatment *in vitro* via nanostructurally constrained diffusion of gold nanorods (GNRs) monitored by polarization-sensitive optical coherence tomography (PS-OCT).

Approach: Using PS-OCT, we quantified GNR translational (D_T) and rotational (D_R) diffusion coefficients within polyethylene oxide solutions (0 to 3 wt. %) and human bronchial epithelial cell (hBEC) mucus (0 to 6.4 wt. %). Interpolation of D_T and D_R data is used to develop an assay to quantify mucus concentration. The assay is demonstrated on the mucus layer of an air–liquid interface hBEC culture during HTS treatment.

Results: In polymer solutions and mucus, D_T and D_R monotonically decrease with increasing concentration. D_R is more sensitive than D_T to changes above 1.5 wt. % of mucus and exhibits less intrasample variability. Mucus on HTS-treated hBEC cultures exhibits dynamic mixing from cilia. A region of hard-packed mucus is revealed by D_R measurements.

Conclusions: The extended dynamic range afforded by simultaneous measurement of D_T and D_R of GNRs using PS-OCT enables resolving concentration of the bronchial mucus layer over a range from healthy to disease in depth and time during HTS treatment *in vitro*.

Keywords: optical coherence tomography; polyethylene oxide; mucus; gold nanorods; particle diffusion

Paper 230339GRR received Oct. 26, 2023; revised Apr. 17, 2024; accepted Apr. 18, 2024; published Apr. 30, 2024.

*Address all correspondence to Amy L. Oldenburg, aold@physics.unc.edu

1 Introduction

In biomedical research, it is of great importance to assess the nanostructure of biomaterials as it relates to disease progression and transport. For instance, tissue engineers are particularly interested in characterizing the nanostructure of biomimetic scaffolds, as it provides mechanical cues for cellular behavior and function.[1] Monitoring alterations in pore size, which occur when the nanostructure of the extracellular matrix (ECM) is remodeled during disease progression or regression,[2,3] can aid in tracking treatment efficacy.[4] Understanding the diffusion of nanoparticles within nanostructures can also lead to new applications for drug delivery. For example, the barrier properties of the biopolymeric meshwork of mucus inform the design of drug delivery systems for the lung epithelium.[5–7] Mucus nanostructure is also an important marker of lung health: in pulmonary diseases such as cystic fibrosis (CF) and chronic obstructive pulmonary disease (COPD), mucus becomes significantly dehydrated, causing disruption of the mucociliary clearance system (MCC),[8–11] which is the primary defense mechanism responsible for trapping and clearing inhaled pathogens from the respiratory system.[12–16] The increase in mucus solids concentration (wt. %) as it becomes dehydrated is directly associated with decrease in nanopore size within the mucus macromolecular meshwork. To counteract the dehydrated mucus' impairment of the MCC, mucus-thinning therapies such as aerosolized hypertonic saline (HTS) are commonly administered.[17,18] Although HTS is a low-cost and easily administered treatment,[18,19] its effectiveness in improving MCC remains uncertain due to patient-to-patient variability and conflicting therapeutic outcomes.[18,20,21] Here we propose a method, based on nanoparticle probe diffusion, for measuring mucus concentration *in situ* and potentially *in vivo* that may provide new insights for improving mucus-thinning therapies.

Scanning electron microscopy (SEM), transmission electron microscopy (TEM), and confocal microscopy are commonly used to assess nanopore size due to their high resolution.[22–26] However, these techniques require segmentation for pore size measurements, generally require staining and, for electron microscopy, additional sample preparation. In comparison, an emerging technique involves measuring the diffusion rate of nanoparticles added to an aqueous macromolecular medium where they are weakly constrained due to intermittent and nonadherent collisions with the macromolecules.[27] This technique offers a promising alternative to traditional imaging methods, as it allows for minimally invasive measurement of the nanopore size distribution and subsequent estimation of the concentration of solids without the need for staining or segmentation. Plasmonic gold nanorods (GNRs) are particularly amenable to this technique because their optical resonance provides a large optical signal from particles that are sufficiently small (<100 nm) to access pores within a macromolecular medium that is well above the overlap concentration, as relevant to biomaterials.

Traditionally, the diffusion of nanoparticles is measured using dynamic light scattering (DLS). GNRs have been assessed via DLS and found to have predictable rotational and translational diffusion rates in water and aqueous glycerol solutions,[28,29] and diffusion of GNRs or related rod-like particles have been proposed for material characterization of polymer solutions.[30,31] However, none of these studies have exploited the plasmonic resonance of GNRs to increase detectability within optically dense materials. Furthermore, an imaging platform such as optical coherence tomography (OCT) is particularly advantageous for performing depth-resolved DLS in biomaterials due to its increased depth penetration and small sample volume requirement.[32,33] Our group's prior efforts have combined these two concepts, demonstrating DLS-OCT at the longitudinal surface plasmon resonance of GNRs to spatially resolve rotational[34] and translational[27] diffusion rates. In addition, the rapid speckle fluctuation rates exhibited by GNRs (with autocorrelation decay times typically <10 ms) enable real-time imaging of GNR diffusion via DLS-OCT. We have dubbed this method diffusion sensitive optical coherence tomography (DS-OCT) and have shown how it reveals temporally and spatially resolved changes in the nanostructure of polymer solutions, collagen, extracellular matrices, and well-hydrated *ex vivo* pulmonary mucus.[27,35,36]

DS-OCT requires the collection of both co-(HH) and cross-(HV) polarized light scattering from the sample in order to compute both translational (D_T) and rotational (D_R) diffusion rates of GNRs. Our previous work in pulmonary mucus focused only on computation of D_T as an indirect measure of mucus solids concentration (wt. %). By collecting D_T in stationary mucus samples,

an interpolation curve relating D_T to concentration was exploited to depth- and time-resolve concentration within the mucus layer of an *in vitro* human bronchial epithelial cell (hBEC) model during treatment by hypertonic and isotonic salines.[35] However, our methods were unable to extend to dehydrated, disease-like mucus concentrations >3.5 wt. %. In this article, for the first time, we address this limitation by monitoring both D_T and D_R together, showing the interplay of how these two types of diffusion change as a function of sample concentration. This report begins by presenting experiments conducted in polyethylene oxide (PEO) solutions due to their utility in mimicking the meshwork of pulmonary mucus.[37] We first quantify D_T and D_R of GNRs in PEO solutions with concentrations ranging from those that weakly to moderately constrain the GNRs. We then extend our experiments to human bronchial epithelial (hBE) mucus, measuring D_T and D_R over a dynamic range of concentrations from hydrated and deemed "healthy" states (<2 wt. %) to more severely dehydrated "diseased-like" states (up to 6.4 wt. %). Importantly, as we demonstrate, the additional computation of D_R allows one to extend the dynamic range of available mucus concentrations to 6.4 wt. %. Finally, using a model developed from the hBE mucus experiment results, we estimate the concentration change over depth and time in air–liquid interface (ALI) hBEC cultures treated with HTS.

2 Materials and Methods

2.1 Polarization Sensitive OCT System

To track both translational and rotational diffusions, a key component of the experimental setup is the polarization sensitive signal collection of the OCT system. A detailed description of our custom polarization sensitive spectral domain OCT system can be found in the previous literature,[34] but here we provide a brief overview. The system utilizes an 800 nm center wavelength Ti:Sapphire laser (Griffin; KM Labs) with a 120 nm bandwidth as its light source, as shown in Fig. 1. The incident beam on the sample is horizontally polarized, whereas the reference beam as it returns from the retroreflector is linearly polarized at 45 deg (equal parts horizontal and vertical components) after double pass through a quarter wave plate. Light scattered from the sample interferes with the reference beam and the resulting co-polarized (HH: horizontal in and horizontal out) and cross-polarized (HV: horizontal in and vertical out) components are separated by a polarizing beam splitter and directed to a custom spectrometer. The spectral components of both polarization channels are dispersed by a diffraction grating and simultaneously imaged onto each half of a 4096-pixel line scan camera. The OCT system has an axial resolution of 3 μm and a transverse resolution of 12 μm in air, and the power directed on the samples was ~3.0 mW. The depth of focus is 283 μm. A-line rates were either 25 or 62.5 kHz as indicated in each experiment below.

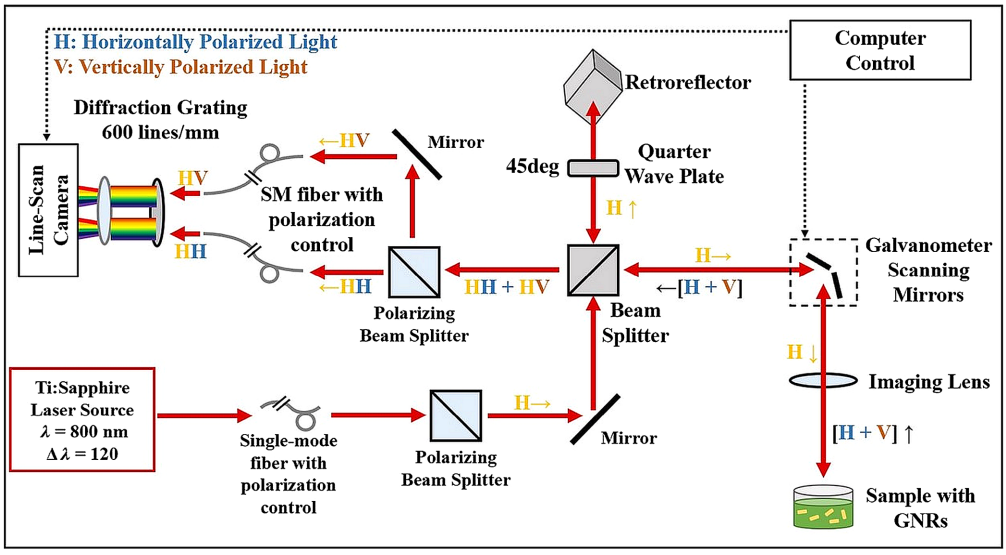

Fig. 1 PS-OCT system schematic.

2.2 Diffusion Coefficient Calculations

As a brief review of DS-OCT analysis methods, as previously described in Ref. 27, DS-OCT consists of collecting M-mode OCT images of a GNR-laden sample to depth-resolve (z) translational (D_T) and rotational (D_R) diffusion coefficients. M-mode OCT images can then be collected at varying lateral positions (x) or at successive times (t) to construct a cross-sectional ($x-z$) or dynamic ($t-z$) image of D_T and D_R; in this study, we perform cross-sectional imaging on stationary samples (PEO, mucus) and dynamic imaging on the mucus layer of *in vitro* ALI hBEC cultures.

For each M-mode OCT image, comprised of A-lines sampled at times t_s, the co-(HH) and cross-(HV) polarized complex analytic OCT signals, $\tilde{S}_{\mathrm{HH}}(t_s;z)$ and $\tilde{S}_{\mathrm{HV}}(t_s;z)$, respectively, are computed from raw OCT data by standard methods. At each z position, the time averages are subtracted, then the normalized temporal autocorrelations $(g_{\mathrm{HH}}(\tau;z), g_{\mathrm{HV}}(\tau;z))$ are computed. To suppress noise, the autocorrelations are then averaged in depth windows of 20 pixels or less; each window is considered a region of interest (ROI). By the Siegert relation, these second-order autocorrelations are equated to first-order autocorrelations $g^{(1)}(\tau;z)$, which, for GNRs at their longitudinal resonance, are related to D_T and D_R as follows:[35]

$$g^{(1)}_{\mathrm{HH}}(\tau;z) = \frac{5}{9}\exp(-q^2 D_T(z)\tau) + \frac{4}{9}\exp(-6D_R(z)\tau)\exp(-q^2 D_T(z)\tau), \tag{1}$$

$$g^{(1)}_{\mathrm{HV}}(\tau;z) = \exp(-6D_R(z)\tau - q^2 D_T(z)), \tag{2}$$

where $q = 4\pi n/\lambda_0$, n is the refractive index of the medium, and λ_0 is the central wavelength of the PS-OCT system. From a linear combination of Eqs. (1) and (2), we calculate the isotropic autocorrelation $g_{\mathrm{ISO}}(\tau;z)$, which isolates the D_T term as follows:

$$g^{(1)}_{\mathrm{ISO}}(\tau;z) = \frac{9}{5}g^{(1)}_{\mathrm{HH}}(\tau;z) - \frac{4}{5}g^{(1)}_{\mathrm{HV}}(\tau;z) = \exp(-q^2 D_T(z)\tau). \tag{3}$$

Under our experimental conditions, the $1/e$ decay time associated with D_T is much longer than that associated with D_R, which simplifies Eq. (2) to isolate the D_R term as

$$g^{(1)}_{\mathrm{HV}}(\tau;z) \approx \exp(-6D_R(z)\tau). \tag{4}$$

Decay times τ_{ISO} and τ_{HV} are extracted by fitting Eq. (3) for $\tau \le \tau_{1/e}$ and Eq. (4) for $\tau \le \tau_{1/e^2}$, where $\tau_{1/e}$ and $\tau \le \tau_{1/e^2}$ are the delay times at which $g^{(1)}$ falls below $1/e$ and $1/e^2$, respectively; this excludes noisy tails in the autocorrelations from the analysis. One exception to this rule was PEO solutions with concentrations >1.5%, for which a fit range for Eq. (4) only up to $\tau_{1/e}$ was used. For *in vitro* hBEC cultures, a dynamic τ_{ISO} threshold was applied such that a fit range of $\tau \le \tau_{1/e^2}$ was used if fittings had fewer than 4 data points. For all fittings, if fewer than 4 data points were available, the ROI was excluded from further analysis. Also the zero-delay point $g(\tau = 0)$ was excluded from all fittings to avoid the contribution of shot noise.

Several criteria were used to determine which ROIs were valid for analysis. Criterion 1 is a top surface detection method to exclude ROIs above the sample or too close to the top surface, which exhibits a strong specular reflection. For PEO and stationary mucus samples, valid ROIs start 15 pixels below the top surface detected (1 pixel $\approx$ 1.5 μm in depth) and 5 pixels below for the hBEC cultures. ROIs are 20 pixels in depth for stationary mucus and 3 pixels in depth for hBEC cultures. Criterion 2 excludes ROIs that are below an average co-polarization (HH) signal threshold above the background noise. Criterion 3 excludes ROIs that do not exhibit valid decay times discussed in Ref. 36. Briefly, we reject ROIs where the decay anisotropy $\tau_{\mathrm{ISO}}/\tau_{\mathrm{HV}} < 1.5$, because dynamic scattering from GNRs exhibits higher decay anisotropy. Additionally, τ_{ISO} and τ_{HV} must lie within the dynamic range of the OCT system (significantly longer than the sampling time and shorter than the total acquisition time). Criterion 4 applies a threshold for autocorrelation fits based on the coefficient of determination (R^2), for PEO solutions $R^2 > 0.88$ and for stationary mucus $R^2 > 0.90$. Criterion 5 was applied only to PEO and stationary mucus samples, where all diffusion coefficients more than five standard deviations from the mean were assessed visually for air bubbles and other imaging artifacts and manually excluded if appropriate.

The fourth and fifth criteria were not applied to *in vitro* hBEC culture studies because mucus hydration was expected to be heterogeneous and dynamically changing.

2.3 Gold Nanorods

GNRs stabilized by cetyltrimethylammonium bromide were synthesized following an established protocol.[38] The GNRs were coated with a 2 kDa molecular weight polyethylene glycol (PEG) methyl ether thiol (Sigma Aldrich) to prevent them from adhering to polymer and mucin macromolecules.[39] Three batches of GNRs were used in the experiments reported. Transmission electron microscopy (TEM) was performed on each batch to measure the gold core size distributions and PEG coating thicknesses. The mean core sizes were 68×19 nm for batch 1, 70×22 nm for batch 2, and 80×22 nm for batch 3. The thickness of the PEG coating has been measured previously as ~0.5 nm, which is half of the distance between the sides of nanorods that have dried aligned next to each other on the TEM substrate.[27] The sizes of the GNRs were chosen to be on the same scale as the nanopores of mucus (~0.2 to 1 μm[40]). Therefore, their Brownian motion is expected to be hindered by the mucus macromolecules, and corresponding diffusion rates are expected to depend on the mucus concentration. The hydrodynamic radius (R_H) of the batches, ~19,22, and 24 nm, respectively, is calculated using GNR length (L) and width (W) according to the following equation:[27]

$$R_H = \frac{L}{2\left(\ln\left(\frac{L}{W}\right) + 0.312 + 0.565\left(\frac{W}{L}\right) - 0.1\left(\frac{W}{L}\right)^2\right)}. \quad (5)$$

2.4 Sample Preparations and Experimental Procedures

2.4.1 *Polymer samples*

PEO of molecular weight (M_W) 4 MDa was prepared into 5 wt. % stock solutions. To prepare a stock solution, PEO powder was stirred constantly in 80°C distilled water for 1 week. From the stock solution, samples ranging from 0 to 3 wt. % solids were prepared. GNRs (batch 1: 68×19 nm) were added to each sample to a final concentration of 1% solids by volume, which is low enough to avoid significant contributions from particle–particle collisions. Polymer solutions were imaged in polystyrene microwells with the PS-OCT system. For all trials, cross-sectional ($x - z$) B + M-mode images (3 mm × 1.5 mm in $x \times z$ in the sample) comprised of 30 M-mode images with 30,000 A-lines each were collected sequentially at a line rate of 62.5 kHz. Samples were imaged sequentially at room temperature.

2.4.2 *Mucus samples*

The stock mucus samples were harvested from hBEC cultures and diluted to concentrations ranging from 1 to 6.4 wt. % with 1× distilled phosphate buffered saline (DPBS) as previously described.[41] GNRs were mixed into individual mucus samples to a final concentration of 1% volume fraction. GNR batch 2 (70×22 nm) was used in both trials 1 and 2. Samples were imaged in polystyrene microwells with the PS-OCT system. Samples of each trial were imaged sequentially at room temperature. For each sample, cross-sectional ($x - z$) B + M-mode images were collected (3 mm × 1.5 mm in $x \times z$ in the sample) comprised of 30 M-mode images with 30,000 A-lines each, collected sequentially at a line rate of 62.5 kHz. Each sample was imaged in two elevationally displaced (y) locations for greater spatial averaging, therefore comprising a total of 60 lateral sites sampled on each of the 2 samples at each concentration.

2.4.3 *ALI cell cultures*

Calu-3 cells were cultured under ALI conditions.[42,43] After 10 days, when there was adequate lumenal mucus accumulation, cells were maintained at ~37°C in HEPES-buffered HBSS-based solution (basolateral solution) for imaging. A 10 μL isotonic saline and GNR mixture was premixed to contain ~1% by volume batch 3 GNRs (80×22 nm) and deposited 6 h before OCT imaging. After initial images were collected, a 10 μL HTS and batch 3 GNR mixture, ~1% by

volume to maintain existing concentration of GNRs in the surface layer, was deposited on top of the cell culture. The cell culture was imaged near the well wall at a 10-to-20-deg angle to avoid imaging the meniscus. 99 total M-mode images comprised of 4000 A-lines were collected at a line rate of 25 kHz all at the same transverse location in the sample. The dynamic $(t - z)$ M-mode images were collected every 3.3 s for 4.5 min, and then every 13.3 s for an additional 4 min.

3 Results

3.1 Diffusion Coefficients of GNRs in Polyethylene Oxide Solutions

The first set of experiments involved measuring GNR diffusion rates in PEO solutions because they are easily accessible, and at Megadalton molecular weights their nanostructure can closely resemble that of mucus.[37] Figure 2 summarizes these measurements, which were spatially resolved within $x - z$ cross sections of PEO solutions of varying concentrations, then averaged as described above to provide a single value of D_T and D_R for each concentration. The top panel of Fig. 2(a) illustrates the concentration-dependence of the D_T of GNRs in 4 MDa PEO, which exhibits a similar trend as in our previous report using 1 MDa PEO samples with differently sized GNRs:[27] D_T in solvent (distilled water) is ~8.5 $\mu m^2/s$ and decreases rapidly as concentration increases. At concentrations higher than 1 wt. %, D_T slows down to <1 $\mu m^2/s$. The middle panel of Fig. 2(a) shows the rotational diffusion rate of GNRs measured within the same samples as translational diffusion. The concentration dependence of D_R in 4 MDa PEO exhibits the same trend observed in D_T such that diffusion is hindered by increasing concentration. However, in

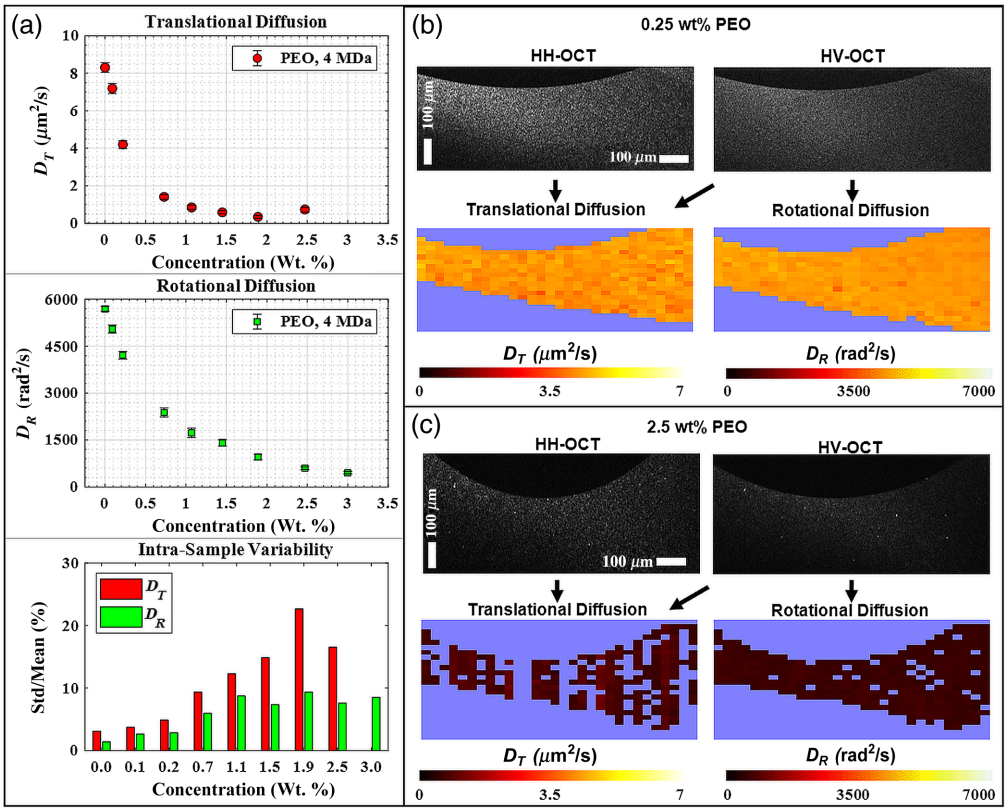

Fig. 2 GNR diffusion in aqueous 4 MDa PEO solutions. In the top panels of (a), D_T and D_R are plotted as a function of PEO solids concentration. In many cases, error bars are not visible due to small standard deviation size. Zero concentration represents GNR diffusion in solvent (distilled water). In the bottom panel, intrasample variability is presented as the percent ratio of the standard deviation to the mean for both D_T and D_R. In panels (b) and (c), co-polarized (HH) and cross-polarized (HV) B-mode images of the 0.25 and 2.5 wt. % PEO solutions are displayed along with corresponding D_T and D_R values within each ROI derived from B + M-mode images; excluded ROIs based on thresholding criteria described in the methods are displayed as the background color.

contrast with the D_T results, the decay of D_R with concentration is less rapid, and D_R continues to decrease across all higher concentrations. D_R is >5000 rad^2/s in solvent and is reduced by a factor of 10 at our highest sample concentration reported (3 wt. %). As shown in the lower panel of Fig. 2(a), in lower concentration samples (<1 wt. %), the variability (or precision) of D_T and D_R is <10%. The intrasample variability is determined by dividing the standard deviation by the mean and expressing the result as a percentage, which is often referred to as the coefficient of variation. At higher concentrations, the variability of the D_T measurements increases well over 10%, whereas D_R measurements maintain low variability across all samples. Figures 2(b) and 2(c) display examples of spatially resolved diffusion measurements at low and high concentrations of PEO. Both D_T and D_R diffusion maps appear to be homogeneous with no spatially varying noise, which is consistent with PEO samples being well-mixed. However, in the higher concentration sample of Fig. 2(c), D_R is defined in nearly twice the number of ROIs defined by D_T.

The magnitude of the reduction in GNR diffusion in PEO solutions compared to solvent depends on the degree to which the GNRs are confined by the PEO meshwork. The relative degree of confinement may be thought of in terms the size of the hydrodynamic radius of the GNRs, R_H, compared to the correlation length of the polymer solution ξ. In the prior work, we defined a weakly constrained regime as one where D_T was reduced by less than a factor of 10 from that of solvent and found that this occurred when $R_H/\xi < 2.2$ in 1 MDa PEO Ref. 27. Experiments in 4 MDa PEO, we observe a reduction in D_T by a factor of 10 at PEO concentrations ≥1.1 wt. %, which, given an R_H of 19 nm for this nanorods batch and ξ of 14 nm for 4 MDa PEO at 1 wt. %, corresponds to a weakly constrained regime defined by $R_H/\xi < 1.4$. For concentrations above 1.1 wt. %, which we will consider to be strongly constrained, D_T was no longer monotonically decreasing and could not be extracted at the highest concentration of 3.0 wt. %. In comparison, D_R continued to monotonically decrease for increasing concentration in the strongly constrained regime, which effectively extends the dynamic range of measurable PEO concentrations to 3.0 wt. % and possibly further. Added support for the ability to extend the dynamic range is seen by assessing the intrasample variability, where fine D_T and D_R precision is evident in the weakly constrained regime, and only D_R precision is fine in the strongly constrained regime.

There are several potential explanations for the varying responses of D_T and D_R versus PEO concentration. First, D_T measurements tended to exhibit lower R^2 values from autocorrelation fittings; this caused many ROIs to be rejected via criterion 4 above where the R^2 threshold was applied, as observed in Fig. 2(c) at 2.5 wt. %; it is also the reason D_T could not be extracted at the highest concentration measured (3.0 wt. %). We believe that the lower R^2 for D_T is either due to the longer τ_{ISO} values at high concentrations, which become a significant fraction of the measurement time, causing noise artifacts in the autocorrelation traces, or possibly because the strongly constrained GNR motion no longer fits a model that can be described by simple diffusion. In comparison, D_R depends only upon τ_{HV}, which is always shorter than τ_{ISO} for the GNRs in our experiments due to decay anisotropy;[36] as GNR confinement increases and decay times increase, the smaller τ_{HV} better remains within the dynamic range of the measurement compared to τ_{ISO}. The fact that D_R is more easily measurable may also suggest a fundamental difference in how diffusive prolate particles rotate versus translate during strong confinement in polymeric solutions, an area of active research.[44]

3.2 Diffusion Coefficients of GNRs in Stationary Pulmonary Mucus

In our previous publications,[27,35] we reported that D_T is sensitive to hBE mucus concentrations ≤2.5 wt. %, both stationary and on actively transporting hBE cultures (*in vitro*). Mucus ≤2 wt. % is considered well-hydrated and would be expected during a state of "healthy" pulmonary mucus production. To extend the capability of DS-OCT to measure the lower mucus hydration levels associated with pulmonary disease-like states, we must perform diffusion experiments on more heavily dehydrated mucus samples (>3 wt. %). Here we expand our investigation of GNR diffusion to a broader range of mucus concentration, up to 6.4 wt. %, and report values of D_R in hBE mucus for the first time.

As shown in Fig. 3(a), while trial 2 tended to exhibit higher D_T and D_R values at all mucus concentrations relative to trial 1, similar concentration-dependent trends were observed overall.

In mucus samples below 2 wt. %, D_T quickly decreases with respect to concentration while remaining above 2 $\mu m^2/s$. For GNRs in dehydrated mucus (>2 wt. %), we observe a general trend that D_T slows at smaller increments with increasing concentration and plateaus at ~0.5 $\mu m^2/s$ [Fig. 3(a)]. In well-hydrated samples, D_R retains a significant fraction of its value in solvent, above ~3000 rad^2/s, then gradually decreases with further increases in mucus sample concentration. At the highest reported concentration, D_R is calculated to be ~1000 and ~1500 rad^2/s in trials 1 and 2, respectively. Across all reported sample concentrations, outside of the solvent data, the variance in D_R is less than half of that observed in D_T. D_T intrasample variability is over 10% in all reported concentrations over 1 wt. %, whereas D_R variability remains under 10%.

Overall, the trends in D_T and D_R versus mucus concentration closely mirror those observed in PEO solutions. If we define, as for the PEO experiments above, a weakly constrained regime of GNR diffusion as that when D_T is $\geq 1/10$ the value in solvent, GNRs transition to being strongly constrained when mucus concentration exceeds ~4.5 wt. %. However, D_R continues to be sensitive to mucus concentration in this strongly constrained regime. Also, similar to results in PEO, diffusion colormaps of the highest concentration sample in Fig. 3(c) show that there are multiple ROIs where D_R is defined while D_T is not (criterion 4). We note that samples in trials 1 and 2 were mixed under slightly different temperatures, potentially contributing to the observed differences in D_T and D_R. The higher concentration samples are prone to air bubbles during the mixing process, an example of which can be seen in Fig. 3(c). Large areas of rejected ROIs are due to air bubbles.

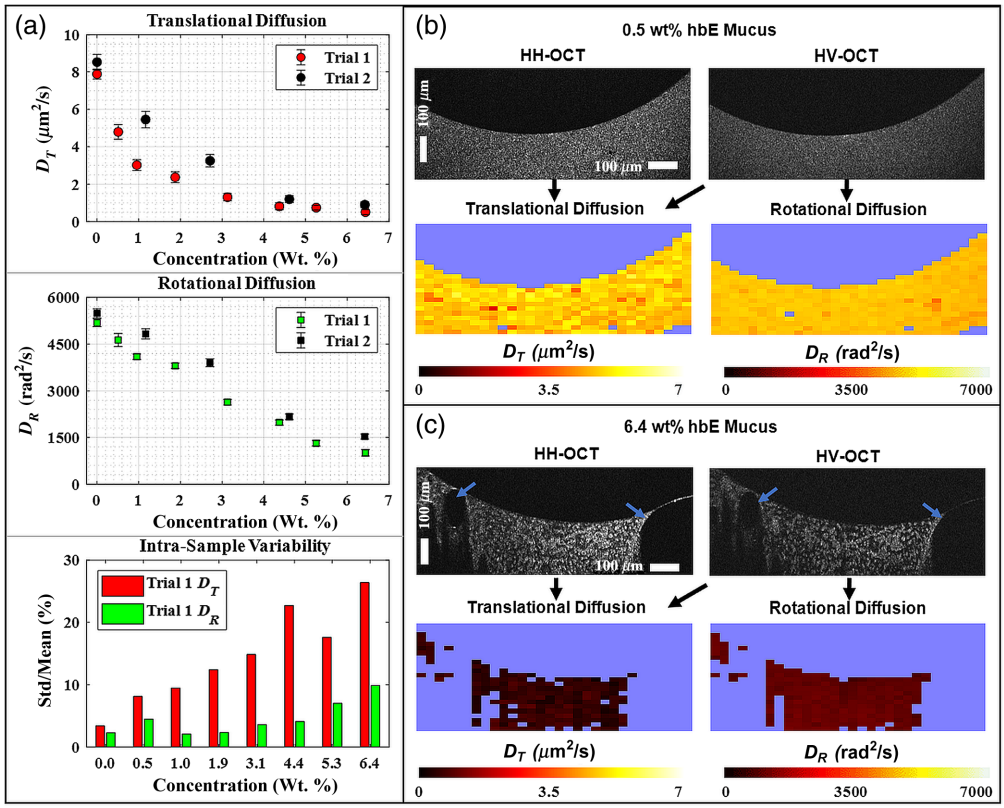

Fig. 3 GNR diffusion in hBE mucus sample. In the top panels of (a), D_T and D_R are plotted as a function of mucus solids concentration. In many cases, error bars are not visible due to small standard deviation size. Zero concentration represents GNR diffusion in solvent (DPBS). In the bottom panel, intrasample variability is presented as the percent ratio of the standard deviation to the mean for both D_T and D_R. (b), (c) Co-polarized (HH) and cross-polarized (HV) B-mode images of the 0.5 and 6.4 wt. % hBE samples are displayed along with corresponding D_T and D_R values within each ROI derived from B + M-mode images; excluded ROIs based on thresholding criteria described in the methods are displayed as the background color. (c) Multiple ROIs are rejected due to air bubbles (indicated by blue arrows) in the 6.4 wt. % sample.

Although D_T measurements are a valid tool for assessing the nanostructure of well-hydrated mucus samples, these results with mucus point to D_R being more sensitive to the concentration of dehydrated mucus samples. Incorporating our previously published translational diffusion in hBE mucus results in Ref. 27 and the above reported hBE experiments, we can define an assay for estimating the concentration of mucus given diffusion coefficient measurements. We first normalized all diffusion coefficients with respect to the diffusion coefficient in solvent measured on the same day, $D_{\text{norm}} = D/D_{\text{solvent}}$. A linear regression was then taken of $D_{T,\text{norm}}$ versus concentration over a well-hydrated range (0 to 2 wt. %), resulting in

$$\text{wt.}\% = -2.75 D_{T_{\text{norm}}} + 2.53, \tag{6}$$

with $R^2 = 0.86$. Similarly, a linear regression of $D_{R,\text{norm}}$ over all concentrations (0 to 6.4 wt. %) was found to be

$$\text{wt.}\% = -8.62 D_{R_{\text{norm}}} + 8.14, \tag{7}$$

with $R^2 = 0.95$. Further details on this regression may be found in the Supplementary Material.

To apply this assay, we collect D_T and D_R measurements in a mucus sample and solvent (saline), then compute weight percents from Eqs. (6) and (7). If the concentration falls between -0.5% and 2% for D_T, or between 1% and 8% for D_R (extrapolating somewhat from the maximum measured value of 6.4 wt. %), we consider it valid and exclude values that fall outside these ranges. In the case where we have valid concentration values from both D_T and D_R, we take the average. One limitation of this method is the potential variation in R_H values among different batches of GNRs. To help account for potential nanorod size variability in D_T measurements, we incorporated three GNR batches with distinct sizes when calculating the D_T trendlines. The GNR batch used in this experiment has a size of 70×22 nm with a corresponding R_H of 22 nm. The additional two batches of GNRs incorporated from our previous publication,[27] sized 83×22 nm and 62×10 nm, had corresponding R_H of 24 and 19 nm.

3.3 Diffusion Coefficients of GNRs on In Vitro Mucus Under HTS Treatment

To mimic the airway epithelium physiology, Calu-3 cells were cultured under ALI conditions. The cell cultures were imaged with PS-OCT immediately before and over the course of 8.5 min after treatment with HTS. The mucus layer, which already contained GNRs introduced 6 h prior, was ~300 μm thick before saline introduction. After topically introducing HTS with additional GNRs, the layer was ~500 μm thick. We note that the bottom surface positions shift after the addition of the saline due to the refractive index of the liquid causing added optical delay in OCT. In Fig. 4(a), we observe D_T of GNRs in the mucus layer of the ALI culture over depth and time. We define a depth of zero as the top of the epithelium where mucus is secreted from mucus goblets. Initially D_T is rapid, with rates much higher than 7 $\mu m^2/s$ during HTS introduction.

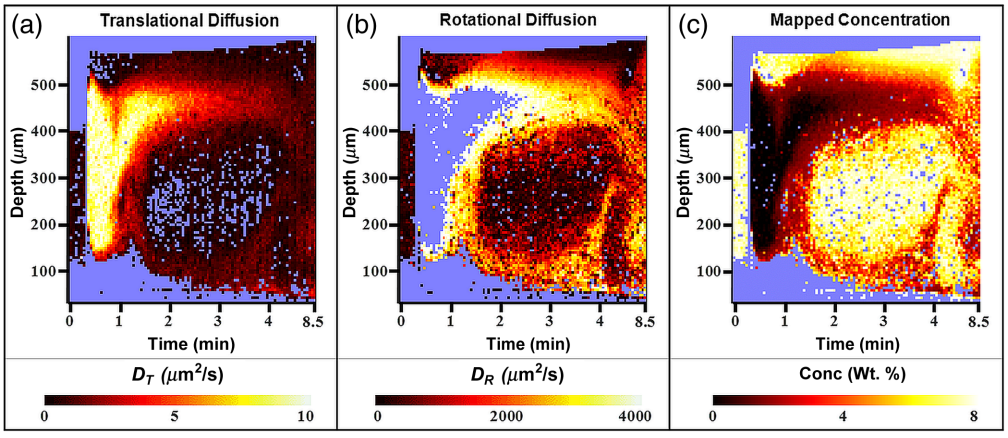

Fig. 4 (a), (b) D_T and D_R in ALI cultures with HTS introduced are color mapped. (c) The diffusion coefficients are mapped to mucus concentration using trendlines produced from stationary mucus experiments. If an ROI had a valid measurement of both D_T and D_R, the calculated concentrations were averaged for a final reported value.

After 1 min, D_T is measurable in ROIs close to the ALI but exhibits an increasing number of invalid ROIs in regions below, closer to the epithelium, likely due to high concentration that is outside the measurement range for D_T. Interestingly, at depths closer to the epithelium, D_T starts to increase after 3 min, whereas it decreases near the top surface, resulting in a more homogenized value of D_T over depth at 8.5 min.

Figure 4(b) reveals the corresponding D_R of GNRs in the mucus layer of the ALI culture. Over the first minute, D_R is largely undefined in between the ALI and the epithelium. The regions of interest that are quantified have high D_R, >3500 rad^2/s. Beyond 2 min, D_R in ROIs close to the surface remain consistently high. Underneath this area, a tall mass of high concentration mucus is revealed by D_R measurements, in which the diffusion is hindered more than those at the ALI. Comparing Figs. 4(a) and 4(b), we see the complementary nature of D_T and D_R, with D_T having fewer invalid ROIs in regions of lower concentration and D_R accessing higher concentration regions; at the same time, the overlapping ROIs of the two appear to follow the same depth- and time-resolved trends.

Using the trendlines defined in Eqs. (6) and (7) for relating D_T and D_R measurements to mucus concentration, in Fig. 4(c), we mapped the concentration of the mucus within the ALI cell culture in depth and time. By employing the new calibration method that exploits the complementary nature of the two diffusion coefficients, we produce a more spatially and temporally contiguous plot. Before HTS is introduced (at time periods $<\sim 20$ s), mucus appears hard-packed within a 400 μm layer. Immediately after HTS is introduced, we observe a $\sim$500 μm layer of liquid that appears to be mostly solvent, then a thin, highly concentrated layer of mucus near the ALI. Over time, high concentration mucus also appears lower down near the epithelium, and the depth-dependent concentration is generally heterogeneous. Between 4 and 8.5 min, the mucus appears to continue to mix and homogenize, likely as a result of ciliary activity on the epithelium, which we have found is more active in response to HTS than to isotonic saline.[35] Bearing in mind that "healthy" mucus is considered to be $\sim$2 wt. %, we see that the mucus layer is nearing but has not quite reached, this value by the end of the experiment. In our previous publication,[35] we observed the reinitiation of the MCC in time-lapse OCT images during HTS treatment on hBEC. These results suggest the promising advantages of incorporating a combination of our advanced DS-OCT-based assay with regular OCT imaging for a comprehensive evaluation of the HTS treatment process in future applications.

4 Discussion

The MCC is the respiratory system's main defense mechanism to inhaled pathogens. Pulmonary diseases, such as CF and COPD, cause mucus to become severely dehydrated and leaves individuals prone to infection. HTS is commonly used to hydrate the mucus to promote better function of the MCC. In this article, we present, for the first time, a method of using translational and rotational diffusion rates of GNRs introduced into the HTS to develop an *in situ* assay of mucus hydration levels. Because mucus is a limited resource, we first quantified diffusion rates in PEO solutions. The rotational diffusion was less hindered than translational diffusion in strongly confining PEO concentrations. A similar effect was observed in stationary hBE mucus samples.

To properly characterize the heterogeneity of a polymeric fluid, a probe must be smaller than the mesh size, or correlation length, of the material but not so small that the probe will never interact with the polymer mesh, i.e., probes must be in a mesoscopic length scale.[45] As a polymeric material, the mesh size of mucus is defined by the concentration and size of the high molecular weight mucin glycoproteins.[46] Published values for the mesh size of mucus between healthy-like concentrations and those associated with airway diseases range between 100 nm and 1 μm.[47] We therefore feel that the 70×22 nm probe size employed by our studies is appropriate to probe the heterogeneity from the nanothrough microscopic length scales. From the measurements in stationary mucus samples, we were able to fit a model to calculate percent weight concentration given D_T and D_R. Applying this model to an hBEC cell culture treated with HTS, we demonstrated that rotational diffusion could provide information of mucus hydration levels up to 6.4 wt. % and may estimate even more highly concentrated mucus as evidenced by extrapolating the regression line out to 8.0 wt. %. The extended mucus concentration range

afforded by this method will enable future insights into the heterogeneity and treatment of disease-like mucus.

Regarding potential *in vivo* use, it is noteworthy that appropriately functionalized GNRs can be biocompatible.[48] GNRs have the potential to be nebulized and administered to the lungs via inhalation. Upon delivery, we would expect them to disperse throughout a highly concentrated mucus layer within minutes. Importantly, GNRs are not expected to penetrate the lung epithelium based upon their size and the exclusion properties of the airway barried[41] and should eventually be cleared by the MCC. However, additional motion stabilization on the millisecond time scale may be needed in order to accurately capture diffusion rates *in vivo*. We note that related efforts to capture ciliary beating with OCT on similar time scales have already been accomplished.[49] Mucociliary transport itself is not expected to significantly impact measurements (motion on the order of 40 to 100 μm/s would be expected to decorrelate a coherence volume in $\geq$0.1 s in our system, which is long compared to the GNR diffusion-associated decay times).[50]

Future applications of measuring both translational and rotational diffusion of GNRs can lie in vast biomedical research areas as biopolymeric meshes are ubiquitous. Overall changes in nanopore size or anisotropy are related to a host of medically relevant processes and diseases. In particular, anisotropic nanostructure may arise from cilia inducing shear on the macromolecular meshwork of mucus or from ECM-altering cells during ECM remodeling processes. For this purpose, we have previously curated a new technique called diffusion tensor OCT (DT-OCT) to determine the anisotropy of a macromolecular pore size using our DS-OCT methods.[51] We also note that, based on these results, the use of a simplified HV-OCT system (in comparison to the HH + HV-OCT system employed here) to measure rotational GNR diffusion alone may prove sufficient to quantify the higher concentrations of the samples investigated in this work. D_R measurements generally exhibited lower intrasample variability (precision), although this does not necessarily imply greater accuracy. At lower concentrations, we found that the HV decay time became too short to be accurately captured by the OCT system's line rate of 62.5 kHz. Further increasing, the line rate would reduce the SNR and ability to detect GNR diffusion. The exclusive reliance on D_R measurements may inadvertently lead to the oversight of low concentration data, and it appears worthwhile to consider the complementary roles of translational diffusion, which is more accurately measured in lower concentration samples, integrated with rotational diffusion for higher concentrations.

5 Conclusions

In summary, quantifying the rotational diffusion of GNRs in conjunction with translational diffusion can provide reasonable estimates of mucus hydration levels, applicable to therapeutic treatment monitoring. By incorporating rotational diffusion measurements, the dynamic range of sample concentration expands to include dehydrated mucus concentrations. This enhanced sensitivity allowed for the development of a real-time assay to study mucus hydration *in situ*.

Disclosures

No conflicts of interest, financial or otherwise, are declared by the authors.

Code and Data Availability

Code and data can be made available upon request to the corresponding author.

Acknowledgments

We would like to acknowledge the assistance of Larry Ostrowski and Patrick Sears at the University of North Carolina at Chapel Hill (UNC). This work was supported by the National Institutes of Health (R21 HL 111968, R21 HL 130901, and R01 HL 123557, Oldenburg, PI), (R01 ES 032730, Oldenburg and Lockett PI), (1 P01 HL 164320 and P30 DK 065988, Hill PI), (R01HL117836, P30DK065988, and UL1RR025747, Ostrowski PI), (NHLBI UH2 HL 123645 and NIDDK DK065988, Kreda PI), the Cystic Fibrosis Foundation (HILL20Y2-OUT, Hill PI), (KREDA10I0, KREDA16XX0 and KREDA13G0, Kreda PI), (KESIME14XX0, Ostrowski PI), (BOUCHE19R0; Kreda, Hill, and Ostrowski PI), the National Science Foundation [(CBET 1351474 and CBET

1803830, Oldenburg PI), (1803785, Tracy PI), and the National Science Foundation Research Triangle Materials Research Science and Engineering Center (DMR-1121107, Tracy)]. This work was performed in part at the Analytical Instrumentation Facility (AIF) at North Carolina State University, which is supported by the State of North Carolina and the National Science Foundation (Award No. ECCS-1542015). This work made use of instrumentation at AIF acquired with support from the National Science Foundation (DMR-1726294). The AIF is a member of the North Carolina Research Triangle Nanotechnology Network (RTNN), a site in the National Nanotechnology Coordinated Infrastructure (NNCI).

References

1. Z. Hao et al., "The scaffold microenvironment for stem cell based bone tissue engineering," *Biomater. Sci.* **5**(8), 1382–1392 (2017).
2. T. R. Cox and J. T. Erler, "Remodeling and homeostasis of the extracellular matrix: implications for fibrotic diseases and cancer," *DMM Dis. Models Mech.* **4**(2), 165–178 (2011).
3. A. S. Abhilash et al., "Remodeling of fibrous extracellular matrices by contractile cells: predictions from discrete fiber network simulations," *Biophys. J.* **107**(8), 1829–1840 (2014).
4. S. Ramanujan et al., "Diffusion and convection in collagen gels: implications for transport in the tumor interstitium," *Biophys. J.* **83**(3), 1650–1660 (2002).
5. W. Poon et al., "A framework for designing delivery systems," *Nat. Nanotechnol.* **15**(10), 819–829 (2020).
6. D. J. Thornton, K. Rousseau, and M. A. McGuckin, "Structure and function of the polymeric mucins in airways mucus," *Annu. Rev. Physiol.* **70**, 459–486 (2008).
7. R. A. Cone, "Barrier properties of mucus," *Adv. Drug Deliv. Rev.* **61**(2), 75–85 (2009).
8. A. E. Tilley et al., "Cilia dysfunction in lung disease," *Annu. Rev. Physiol.* **77**, 379–406 (2015).
9. B. K. Rubin, "Mucus structure and properties in cystic fibrosis," *Paediatr. Respir. Rev.* **8**(1), 4–7 (2007).
10. R. C. Boucher, "Pathogenesis of cystic fibrosis airways disease," *Trans. Am. Clin. Climatol. Assoc.* **112**, 99–107 (2001).
11. R. C. Boucher, "Cystic fibrosis: a disease of vulnerability to airway surface dehydration," *Tr. Mol. Med.* **13**(6), 231–240 (2007).
12. S. H. Randell and R. C. Boucher, "Effective mucus clearance is essential for respiratory health," *Am. J. Respir. Cell Mol. Biol.* **35**(1), 20–28 (2006).
13. M. R. Knowles and R. C. Boucher, "Mucus clearance as a primary innate defense mechanism for mammalian airways," *J. Clin. Investig.* **109**(5), 571–577 (2002).
14. S. Girod et al., "Role of the physicochemical properties of mucus in the protection of the respiratory epithelium," *Eur. Respir. J.* **5**(4), 477–487 (1992).
15. E. Houtmeyers et al., "Regulation of mucociliary clearance in health and disease," *Eur. Respir. J.* **13**(5), 1177–1188 (1999).
16. R. Bansu, E. Stanley, and J. T. Lamont, "Mucin biophysics," *Annu. Rev. Physiol.* **57**, 635–657 (1995).
17. B. E. Tildy and D. F. Rogers, "Therapeutic options for hydrating airway mucus in cystic fibrosis," *Pharmacology* **95**(3–4), 117–132 (2015).
18. D. H. Scott et al., "Mucus clearance and lung function in cystic fibrosis with hypertonic saline," *N. Engl. J. Med.* **354**(3), 241–250 (2006).
19. E. P. Reeves et al., "Inhaled hypertonic saline for cystic fibrosis: reviewing the potential evidence for modulation of neutrophil signalling and function," *World J. Crit. Care Med.* **4**(3), 179–191 (2015).
20. M. A. Mall, "Unplugging mucus in cystic fibrosis and chronic obstructive pulmonary disease," *Ann. Am. Thorac. Soc.* **13**, S177–S185 (2016).
21. V. L. Yap and M. L. Metersky, "New therapeutic options for noncystic fibrosis bronchiectasis," *Curr. Opin. Infect. Dis.* **28**(2), 171–176 (2015).
22. B. S. Schuster et al., "Nanoparticle diffusion in respiratory mucus from humans without lung disease," *Biomaterials* **34**(13), 3439–3446 (2013).
23. F. Y. Zhu et al., "3D nanostructure reconstruction based on the SEM imaging principle, and applications," *Nanotechnology* **25**(18), 185705 (2014).
24. R. Ziel, A. Haus, and A. Tulke, "Quantification of the pore size distribution (porosity profiles) in microfiltration membranes by SEM, TEM and computer image analysis," *J. Membrane Sci.* **323**(2), 241–246 (2008).
25. S. H. Kim et al., "Anisotropically organized three-dimensional culture platform for reconstruction of a hippocampal neural network," *Nat. Commun.* **8**, 14346 (2017).
26. K. H. Kim et al., "TEM based high resolution and low-dose scanning electron nanodiffraction technique for nanostructure imaging and analysis," *Micron* **71**, 39–45 (2015).
27. R. K. Chhetri et al., "Probing biological nanotopology via diffusion of weakly constrained plasmonic nanorods with optical coherence tomography," *Proc. Natl. Acad. Sci. U. S. A.* **111**(41), E4289–E4297 (2014).

28. F. E. Berger Bioucas et al., "Translational and rotational diffusion coefficients of gold nanorods dispersed in mixtures of water and glycerol by polarized dynamic light scattering," *J. Phys. Chem. B* **123**(44), 9491–9502 (2019).
29. R. Nixon-Luke and G. Bryant, "Differential dynamic microscopy to measure the translational diffusion coefficient of nanorods," *J. Phys. Condens. Matter* **32**(11), 115102 (2020).
30. M. Molaei, E. Atefi, and J. C. Crocker, "Nanoscale rheology and anisotropic diffusion using single gold nanorod probes," *Phys. Rev. Lett.* **120**(11–16), 118002 (2018).
31. S. Martín-Martín et al., "Electro-optical study of the anomalous rotational diffusion in polymer solutions," *Macromol. Am. Chem. Soc.* **56**(2), 518–527 (2022).
32. G. Popescu, A. Dogariu, and R. Rajagopalan, "Spatially resolved microrheology using localized coherence volumes," *Phys. Rev. E: Stat. Nonlin. Soft Matter Phys.* **65**(4), 041504 (2002).
33. A. Wax et al., "Path-length-resolved dynamic light scattering: modeling the transition from single to diffusive scattering," *Appl. Opt.* **40**(24), 4222–4227 (2001).
34. R. K. Chhetri et al., "Imaging three-dimensional rotational diffusion of plasmon resonant gold nanorods using polarization-sensitive optical coherence tomography," *Phys. Rev. E: Stat. Nonlin. Soft Matter Phys.* **83**(4–1), 040903 (2011).
35. R. L. Blackmon et al., "Direct monitoring of pulmonary disease treatment biomarkers using plasmonic gold nanorods with diffusion-sensitive OCT," *Nanoscale* **9**(15), 4907–4917 (2017).
36. R. L. Blackmon et al., "Imaging extracellular matrix remodeling in vitro by diffusion-sensitive optical coherence tomography," *Biophys. J.* **110**(8), 1858–1868 (2016).
37. B. Rankin, "Method of providing a synthetic mucus in vivo," United States Patent US 3,767,789 (1973).
38. K. A. Kozek et al., "Large-scale synthesis of gold nanorods through continuous secondary growth," *Chem. Mater.* **25**(22), 4537–4544 (2013).
39. S. R. Mishra and J. B. Tracy, "Sequential actuation of shape-memory polymers through wavelength-selective photothermal heating of gold nanospheres and nanorods," *ACS Appl. Nano Mater.* **1**(7), 3063–3067 (2018).
40. H. Matsui et al., "A physical linkage between cystic fibrosis airway surface dehydration and Pseudomonas aeruginosa biofilms," *Proc. Natl. Acad. Sci. U. S. A.* **103**(48), 18131–18136 (2006).
41. B. Button et al., "A periciliary brush promotes the lung health by separating the mucus layer from airway epithelia," *Science* **337**(6097), 937–941 (2012).
42. S. M. Kreda et al., "Coordinated release of nucleotides and mucin from human airway epithelial Calu-3 cells," *J. Physiol.* **584**(1), 245–259 (2007).
43. S. M. Kreda et al., "Characterization of wild-type and F508 cystic fibrosis transmembrane regulator in human respiratory epithelia," *Mol. Biol. Cell* **16**(5), 2154–2167 (2005).
44. S. Alam and A. Mukhopadhyay, "Translational anisotropy and rotational diffusion of gold nanorods in colloidal sphere solutions," *Langmuir* **31**(32), 8780–8785 (2015).
45. S. K. Lai et al., "Micro-and macrorheology of mucus," *Adv. Drug Deliv. Rev.* **61**(2), 86–100 (2009).
46. D. B. Hill et al., "Physiology and pathophysiology of human airway mucus," *Physiol. Rev.* **102**(4), 1757–1836 (2022).
47. G. A. Duncan et al., "Microstructural alterations of sputum in cystic fibrosis lung disease," *JCI Insight* **1**(18), e88198 (2016).
48. B. C. Tang et al., "Biodegradable polymer nanoparticles that rapidly penetrate the human mucus barrier," *Proc. Natl. Acad. Sci. U. S. A.* **106**(46), 19268–19273 (2009).
49. K. K. Chu et al., "In vivo imaging of airway cilia and mucus clearance with micro-optical coherence tomography," *Biomed. Opt. Express* **7**(7), 2494 (2016).
50. A. L. Oldenburg et al., "Monitoring airway mucus flow and ciliary activity with optical coherence tomography," *Biomed. Opt. Express* **3**(9), 1978–1992 (2012).
51. D. L. Marks, R. L. Blackmon, and A. L. Oldenburg, "Diffusion tensor optical coherence tomography," *Phys. Med. Biol.* **63**(2), 025007 (2018).

Biographies of the authors are not available.